Materials Advances

ROYAL SOCIETY OF CHEMISTRY

PAPER

View Article Online
View Journal | View Issue

Cite this: *Mater. Adv.*, 2026, 7, 3300

Comparison of properties and performance of Eu^{2+}-doped $Ca_6BaP_4O_{17}$, $Ca_4Sr(PO_4)_3Cl$, $NaSrPO_4$ and $Sr_3Al_2O_5Cl_2$ thermometric phosphors

Simon N. Ogugua, * Robin E. Kroon and Hendrik C. Swart *

Received 1st December 2025,
Accepted 24th January 2026

DOI: 10.1039/d5ma01397f

rsc.li/materials-advances

The temperature sensitivity of a luminescent material depends on its thermodynamic properties, such as its activation energy (ΔE). In this work, we demonstrated the dependence of the relative temperature sensitivity (S_r) on ΔE for four thermometric phosphors, namely $Ca_6BaP_4O_{17}$:0.05Eu^{2+} (CBP:Eu), $Ca_4Sr(PO_4)_3Cl$:0.02Eu^{2+} (CSPC:Eu), $NaSrPO_4$:0.04Eu^{2+} (NSP:Eu) and $Sr_3Al_2O_5Cl_2$:0.1Eu^{2+} (SAC:Eu), for which the values of ΔE varied according to SAC:Eu > CBP:Eu > NSP:Eu > CSPC:Eu. The maximum values of S_r behave in a correlated manner, with values of 1.973, 1.452, 0.610 and 0.137% $°C^{-1}$, respectively. At room temperature, the phosphors possessed good S_r values of 1.148% $°C^{-1}$ (SAC:Eu), 0.349% $°C^{-1}$ (CBP:Eu), 0.346% $°C^{-1}$ (NSP:Eu) and 0.089% $°C^{-1}$ (CSPC:Eu), indicating their potential for thermometry applications at near ambient temperatures. This demonstrates that to increase the sensitivity, the value of ΔE should be maximized. The energy gap between the 5d excited state of Eu^{2+} ions and the conduction band minimum, the thermal ionization energy (ΔE_i), showed an irregular relationship with ΔE, likely because ΔE was obtained from data measured at elevated temperatures, whereas the other was obtained from room temperature data. Considering the obtained values of ΔE and ΔE_i, thermal ionization is the dominant mechanism for thermal quenching in CSPC:Eu, NSP:Eu and SAC:Eu, whereas the rate for both thermal ionization and non-radiative crossover relaxation mechanisms is similar in CBP:Eu. The values of the quantum yield for SAC:Eu, NSP:Eu, CBP:Eu, and CSPC:Eu are 35, 23, 19, and 10%, respectively. Factoring in all the obtained values, SAC:Eu demonstrates the best performance among all the phosphors.

1. Introduction

The global temperature sensor market constituted USD 6 billion in 2021, and it is estimated to have a compound annual growth rate of 5.4%, to reach USD 10.6 billion by 2031.[1] Temperature is a variable of critical importance because it governs heat transport and chemical reaction rates in systems and processes, *e.g.*, thermal convection, aerosol systems, biological sensing, and the pathogenesis of diseases such as cancer cells.[2,3] In addition, the brain's local temperature and thermal dynamics can help understand its physiology and be used as a diagnostic tool.[4] Other applications of temperature sensors include metrology, military, home appliances, agriculture, *etc*.

Changes in physical phenomena with temperature, *e.g.*, thermal expansion of substances such as mercury, air, or alcohol, the conductivity or ductility changes of metals, change in infrared reflections, and change in luminescence can be calibrated to readable temperature scales.[5] Temperature sensors can be classified as invasive, non-invasive or semi-invasive based on their mode of interaction with the object of analysis. For invasive or contact systems, the sensor is in physical contact with the object of interest, *e.g.*, gas and liquid-in-glass thermometers, thermocouples and thermistors. Non-invasive or non-contact devices measure an object's temperature without physical contact, *e.g.*, infrared devices. Semi-invasive systems involve coating surfaces with thermally active materials, *e.g.*, thermochromic liquid crystals, paints, and luminescent materials, and observing the changes in their optical properties remotely.[6] The advantages of the semi-invasive over invasive sensors include the ability to work in hazardous environments, *e.g.*, flames or plasmas, and to measure the temperature of moving components, *e.g.*, an automobile piston, a hot jet engine blade, *etc.* Among the semi-invasive temperature techniques, optical techniques (*e.g.*, luminescence thermometry) have a major advantage due to their high temperature resolution of about 0.003 K, which is superior to that of infrared cameras, around 1 K,[7] making it difficult to obtain knowledge of surface characteristics when using infrared cameras.

In luminescence thermometry, the principle is based on the change of the luminescence properties of materials with

Department of Physics, University of the Free State, Bloemfontein, ZA9300, South Africa. E-mail: Oguason@yahoo.com, Kroonre@ufs.ac.za, Swarthc@ufs.ac.za

temperature. This technique has shown enormous advantages over the other techniques, such as the simplicity of the process, better temperature resolution, high acquisition rate, and the ability to operate at the intercellular level. Temperature sensitivity can be obtained from luminescence thermometry using the temporal[8,9] or spectral method.[10–13] Comprehensive information on the different spectral techniques for temperature readout is available.[14,15] A major drawback of the spectral method is that the thermometry is influenced by changes in luminescence excitation conditions or local probe concentrations.[16] In the temporal method, the excitation and signal detection changes do not affect the readouts. However, it is challenging to implement temperature imaging.[17]

The materials commonly used in luminescence thermometry include organic compounds (*e.g.* dyes), metal–ligand complexes, quantum dots, polymeric matrices, and lanthanide complexes.[18] Among luminescence thermometry, phosphor thermometry is based on inorganic compounds called hosts, combined with a small quantity of optically active lanthanides, transition metals or post-transition metals known as dopants. Phosphors possess apparent advantages in the field of *in vivo* imaging, including high brightness (quantum yield), photostability, non-phototoxic, excellent signal-to-noise ratio, and high sensitivity in the biological medium.[18] Unlike quantum dots, the spectral maxima are unaffected by particle sizes and hence do not shift within the investigation region.[19] Some of the demerits of phosphor thermometers include a long decay time between several microseconds to milliseconds, and difficulty achieving uniform nanoparticle sizes. In fluorescence lifetime imaging, the rate of data acquisition depends on the fluorescence lifetime. Short fluorescence lifetimes allow fast data acquisition, while long fluorescence lifetimes slow data acquisition. Nevertheless, each time scale can be measured using different systems, *e.g.* for short lifetime measurements, in the nanosecond scale, fluorescence lifetime imaging uses time-correlated single photon-counting, or phase-modulated detectors and high repetition rates, or modulated excitation sources.[20] For long lifetime measurements, in the microsecond scale, low frame rate gated cameras such as global shutter complementary metal oxide semiconductor (CMOS) or interline-transfer CCDs and low repetition rate pulsed excitation sources are used.[17] For surface phosphor thermometry, kilohertz frame rate CMOS cameras coupled with a single excitation source can resolve decay times of tens of microseconds and longer.[21]

For temperature-dependent of luminescence or lifetime measurements, the luminescence intensity and lifetime values are usually fairly insensitive to temperature changes over an extensive range of low temperatures and show a steep decrease over a narrow temperature range at high temperatures. Therefore, it is vital to produce more phosphor-based thermometers that possess decent temperature sensitivity around room temperatures and physiological temperatures. In some cases, the quenching behaviour of luminescence intensity and lifetime of a phosphor deviates completely in different temperature regions.[22,23] This feature largely depends on the intrinsic properties of the host material and the dopant ion. Among the lanthanide-based phosphors, divalent europium ion (Eu^{2+}) doped materials have shown exceptional thermal sensitivity around ambient temperatures.[24,25] The electronic configuration of Eu^{2+} is $[Xe]4f^7$ with a half-filled f shell. The f shell is shielded by the closed $5s^2$ and $5p^6$ outer shells. The half-filled f shell has an $^8S_{7/2}$ ground state with a $4f^75d^0$ electronic configuration and $4f^65d^1$ excited state.[26] Eu^{2+} is one of the few lanthanide ions (including Ce^{3+}, Pr^{3+} and Sm^{2+}) that emit through 5d–4f transitions. The energy gap between the 4f and 5d levels decreases with an increase in the crystal field strength of a host material. The crystal field strength increases with a decrease in the bond length of the ligands.[27] Generally, as the crystal field experienced by Eu^{2+} ions in a host increases, the position of the emission band maximum shifts to a longer wavelength.[28] This implies that the energy levels of the $4f^75d^0$ ground state and the $4f^65d^1$ excited state of Eu^{2+} are sensitive to the host material – a property which plays a key role in the thermal quenching mechanism.[29] These characteristics of Eu^{2+} ions enable them to emit at different wavelength regions and possess different luminescent lifetimes when incorporated in hosts of distinct structural properties. In most cases, Eu^{2+} doped materials possess a lifetime in the sub-microsecond to a few microseconds range, making them suitable for imaging applications.

We prepared Eu^{2+} doped in different hosts ($Ca_6BaP_4O_{17}$, $Ca_4Sr(PO_4)_3Cl$, $NaSrPO_4$, and $Sr_3Al_2O_5Cl_2$) using the solid-state synthesis method and compared their thermometric properties. These phosphors have been widely studied, with optimum luminescence intensities obtained from $Ca_6BaP_4O_{17}$:$0.05Eu^{2+}$,[8] $Ca_4Sr(PO_4)_3Cl$:$0.02Eu^{2+}$,[30] $NaSrPO_4$:$0.04Eu^{2+}$,[31] and $Sr_3Al_2O_5Cl_2$:$0.1Eu^{2+}$.[25] Given the varying structural properties of these host materials, it is anticipated that Eu^{2+} ions will occupy different energy levels upon incorporation. In addition, these hosts are thermally sensitive across the same temperature range, albeit at different rates. This will result in each material exhibiting unique luminescence and thermal properties at a given temperature within the measured range. We measured the structure, morphologies, and the temperature-dependence of luminescence and lifetime. Eu^{2+} emissions were observed at different wavelength regions (blue, green, and red) from these hosts when excited using the third harmonic of a pulsed Nd:YAG laser (355 nm). The thermometric properties of the phosphors were determined from the temperature-dependent lifetime data, and the graph of temperature parameters, such as the activation energy and relative sensitivity, exhibited a consistent correlation. Additionally, the energy difference between the host conduction bands and the $4f^65d^1$ excited state of Eu^{2+} showed an inconsistent relationship. We also report the quantum yield of the phosphors.

2. Experimental

2.1. Synthesis

The phosphors were prepared using a high-temperature solid-state method. The starting materials for each phosphor were analytical reagents of (i) Ca_6BaP4O_{17}:$0.1Eu^{2+}$–$CaCO_3$ (0.5101 g) $BaCO_3$ (0.5028 g), $CaHPO_4$ (1.3868 g), Eu_2O_3 (0.0448 g),

(ii) $Ca_4Sr(PO_4)_3Cl$:0.03Eu^{2+}–$CaCO_3$ (1.6847 g), $SrCO_3$ (0.3106 g), $SrCl_2H_2O$ (0.3715 g), $(NH_4)_2HPO_4$ (1.6672 g), Eu_2O_3 (0.0149 g) (iii) $NaSrPO_4$:0.05Eu^{2+}–Na_2CO_3 (0.5016 g), $SrCO_3$ (1.3973 g), $(NH_4)_2HPO_4$ (1.2499 g), Eu_2O_3 (0.0666 g) and (iv) $Sr_3Al_2O_5Cl_2$:0.1Eu^{2+}–$SrCO_3$ (1.2415 g), $SrCl_2{\cdot}H_2O$ (0.7422 g), Al_2O_3 (0.4286 g), Eu_2O_3 (0.0091 g). The Eu_2O_3 has a purity of 99.99%. The stoichiometric amount of each starting material was weighed, and acetone was used to make a slurry mixture inside an agate mortar. The mixture was ground using a pestle for about 30 minutes, placed in a crucible boat, transferred to a tube furnace, and annealed in a 95% Ar/5% H_2 atmosphere. $Ca_6BaP_4O_{17}$:0.1Eu^{2+}, $Ca_4Sr(PO_4)_3Cl$:0.03Eu^{2+}, $NaSrPO_4$:0.05Eu^{2+}, and $Sr_3Al_2O_5Cl_2$:0.1Eu^{2+} were annealed at 1000 °C (8 h), 1000 °C (10 h), 850 °C (16 h) and 1000 °C (4 h), respectively. The samples were allowed to cool to room temperature and ground again to obtain fine powders.

2.2. Characterization

A Bruker D8 Advance X-ray diffractometer was used for the structure characterization. The morphologies and the elemental analysis were performed using a Jeol JSM-7800F field emission scanning electron microscope (FE-SEM) fitted with an Oxford X-MaxN 80 energy-dispersive X-ray spectrometer (EDS). The temperature-dependent luminescence and the lifetime were measured by exciting the phosphors using the third harmonic of a pulsed Nd:YAG laser (355 nm, 10 ns, 10 Hz) with a fluence of 1 mJ cm^{-2} (see Fig. 5). The luminescence was recorded using a spectrometer (Acton Research SPro300i, f = 500 mm, 300 grooves per mm), while the lifetime was recorded with a DET100A2 Thorlabs photodetector connected to an oscilloscope. The temperature was varied using a DC power supply and measured using a type K thermocouple (see Fig. 5). The quantum yield (QY) was measured using an integrating sphere incorporated in an FLS980 spectrometer (Edinburgh Instruments) equipped with a 450 W xenon lamp as a steady-state excitation source. A detailed procedure for the QY measurement was reported in ref. 32.

3. Results and discussion

3.1. Structure

The X-ray powder diffraction (XRPD) patterns of the phosphors are shown in Fig. 1. $Ca_6BaP_4O_{17}$:0.05Eu^{2+} (CBP:Eu) phosphor (Fig. 1(a)) crystallized in a monoclinic phase with space group $C2/m$ and the Rietveld refined cell parameters listed in Table 1 agreed well with the standard cell parameters. The unit cell of $Ca_6BaP_4O_{17}$ is shown in Fig. 2(a). The crystal structure comprises two kinds of Ca sites (Ca1 and Ca2) and unique Ba and P sites. Ba is coordinated to twelve O atoms with S2 point symmetry, with an average bond length of 3.04 Å. Each BaO_{12} dodecahedron is connected to two PO_4 tetrahedra by O_3 faces and six PO_4 tetrahedra by O vertices. The Ca1 and Ca2 sites are coordinated to eight and seven oxygen atoms with Cs and C1 point symmetries and average bond lengths of 2.51 and 2.42 Å, respectively. Each Ca site is connected to an isolated O atom (non-P bonded).[33] The ionic radii of Ca in its seven and eight

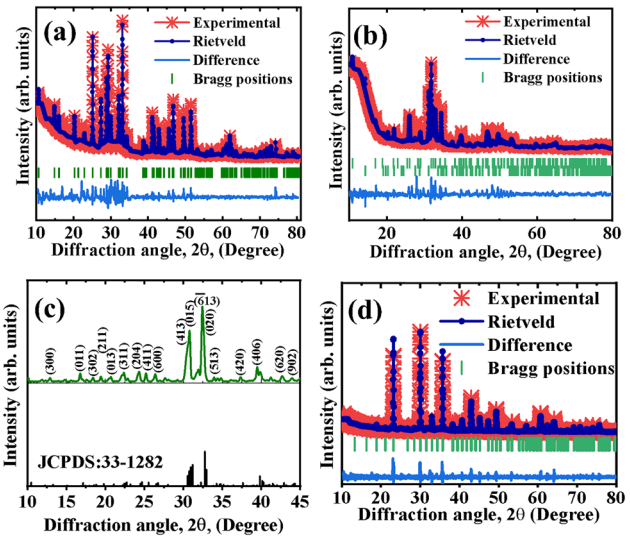

Fig. 1 Rietveld refined XRPD of (a) CBP:Eu, (b) CSPC:Eu, XRPD of (c) NSP:Eu and (d) Rietveld refined XRPD of SAC:Eu.

coordination are 1.07 and 1.12 Å, respectively, which can be randomly occupied by Eu^{2+} with ionic radii of 1.20 and 1.25 Å in the same coordination, respectively.[34]

$Ca_4Sr(PO_4)_3Cl$:0.02Eu^{2+} (CSPC:Eu) crystallized as 92% $Ca_4Sr(PO_4)_3Cl$ single-phase with 8% $Ca_3(PO_4)_2$ impurity phase, and the Rietveld refined XRPD is shown in Fig. 1(b). CSPC:Eu crystallized in a hexagonal phase (with a structure similar to $Ca_5(PO_4)_3Cl$) with a $P63/m$ (176) space group, and the Rietveld refined cell parameters listed in Table 1 matched well with standard cell parameters. The crystal structure of $Ca_4Sr(PO_4)_3Cl$ is represented with the unit cell of $Ca_5(PO_4)_3Cl$ in Fig. 2(b). $Ca_5(PO_4)_3Cl$ has two kinds of Ca^{2+} sites, Ca1 and Ca2, of which Sr^{2+} will replace one in $Ca_4Sr(PO_4)_3Cl$. The Ca1 site is coordinated by nine O atoms, while the Ca2 site is coordinated by six O and two Cl atoms.[35]

$NaSrPO_4$ exhibits multiple phase transitions depending on the annealing temperature. $NaSrPO_4$ can exhibit up to four phase transitions between room temperature and 750 °C.[36] $NaSrPO_4$ can crystallize in an orthorhombic phase,[37] a hexagonal phase,[36] and a monoclinic phase.[38] The XRPD pattern of $NaSrPO_4$:0.04Eu^{2+} (NSP:Eu) showed that it crystallized in a monoclinic phase with a $Pn21a$ space group, matching the ICDD file no. 00-033-1282 of $NaSrPO_4$, Fig. 1(c).[38] The crystallographic data of monoclinic $NaSrPO_4$ are not available in the literature; therefore, we were unable to perform the refinement.

The XRPD pattern of $Sr_3Al_2O_5Cl_2$:0.1Eu^{2+} (SAC:Eu) crystallized in an orthorhombic phase with $P2_12_12_1$ space group, and the Rietveld refined XRPD is shown in Fig. 1(d). The refined cell parameters tabulated in Table 1 matched well with the standard. $Sr_3Al_2O_5Cl_2$ contains three different Sr sites (Sr1, Sr2, and Sr3), and each site is coordinated by five O^{2-} and four Cl^- ligands with differences in the average Sr–O and Sr–Cl bond lengths, Fig. 2(c).[39] Additional Rietveld refinement parameters, including atomic displacement parameters, occupancy, and

Table 1 Crystallographic and refinement parameters of the phosphors

	CBP:Eu		CSPC:Eu		SAC:Eu	
	Prototype	Refined	Prototype	Refined	Prototype	Refined
a (Å)	12.3030(7)	12.2130	9.5200(3)	9.54212	9.5000	9.4176 (9)
b (Å)	7.1045(4)	7.1203	9.5200	9.5311	9.5100	9.3989(6)
c (Å)	11.7160(8)	11.6825	6.8500(3)	6.8913	9.5200	9.3996(6)
V (Å^3)	731.14(4)	734.08	537.644(3)	538.732	860.24	832.05(1)
α (°)	—	—	90.0	90.0	90.0	90.0
β (°)	134.442	134.521	90.0	90.0	90.0	90.0
γ (°)	—	—	120.0	120.0	90.0	90.0
Phase	Monoclinic	Monoclinic	Hexagonal	Hexagonal	Orthorhombic	Orthorhombic
Space group	$C2/m$	$C2/m$	$P63/m(176)$	$P63/m$	$P2_12_12_1$	$P2_12_12_1$
R_p (%)		13.24		14.06		8.48
R_{wp} (%)		16.91		18.35		11.99
χ^2		3.42		5.17		2.82

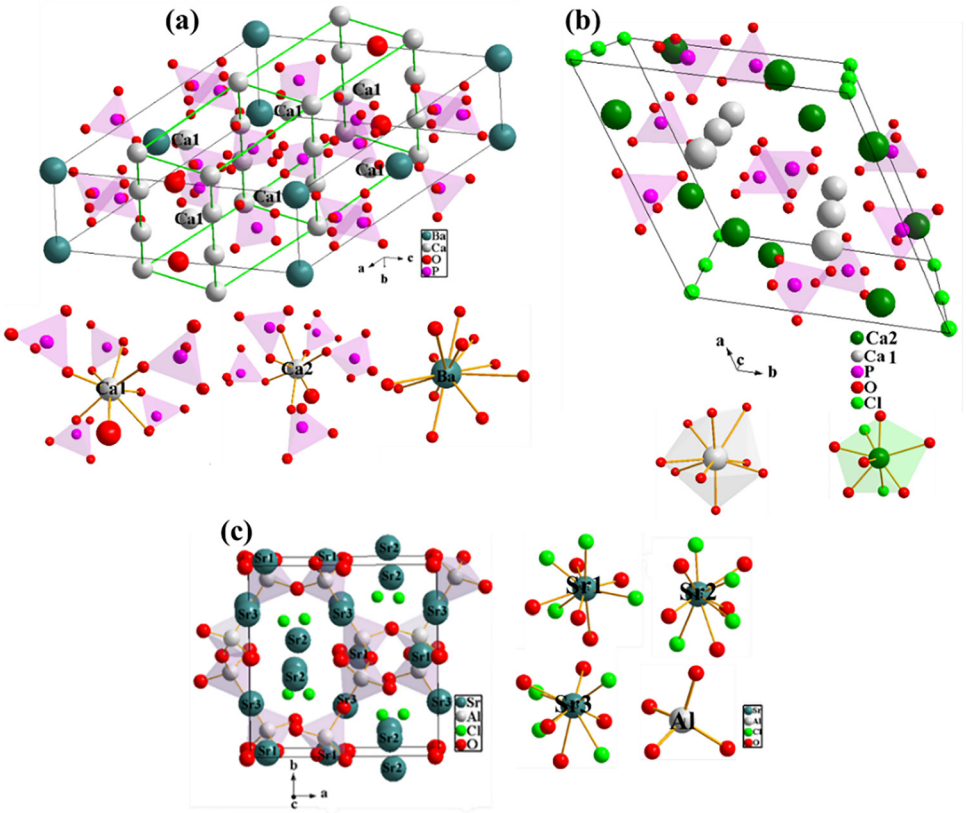

Fig. 2 Crystal structures of (a) CBP, (b) CSPC and (c) SAC hosts.

Wyckoff positions, are detailed in Tables S1–S3 for CBP:Eu, CSPC:Eu, and SAC:Eu, respectively.

3.2. Morphology and elemental composition

The FE-SEM images of the phosphors are shown in Fig. 3(a–d). The images are at the scale of 1 × 1 μm^2. The FE-SEM images of CBP:Eu and CSPC:Eu contain irregular (polyhedral) shaped particles (Fig. 3(a and b)) of various sizes, with an average size of 0.6 and 0.5 μm, respectively, Fig. 3(e and f). The image of NSP:Eu contains agglomerates of spherical particles, Fig. 3(c), with an average size of 0.7 μm, Fig. 3(g). The image of SAC:Eu shows micrometer-sized rod-like particles, Fig. 3(d). The sizes of these particles made them suitable for flow tracing in fluids.[40]

3.3. Elemental analysis

The EDS data in Fig. 4 confirmed the presence of all the expected elements in the materials, including Ca, Ba, P, O and Eu in CBP:Eu, Fig. 4(a); Sr, Ca, P,O, Cl and Eu in CSPC:Eu, Fig. 4(b); Na, Sr, P, O (Eu peak is not visible in the spectrum, but present in Table 2) in NSP:Eu, Fig. 4(c), and Sr, Al, O, Cl, and Eu in SAC:Eu, Fig. 4(d). The C could be from the carbonate precursors used as the starting materials. The elemental compositions of each material are listed in Table 2.

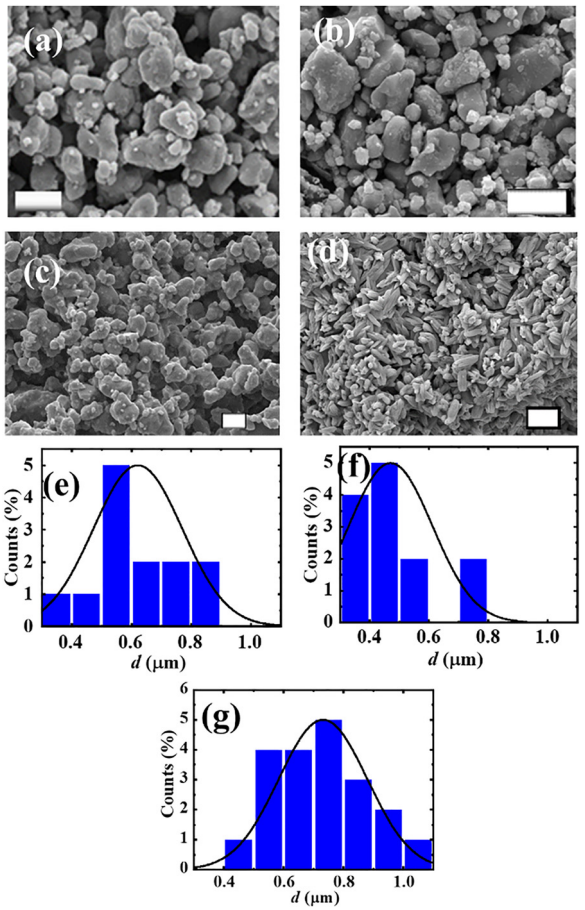

Fig. 3 FE-SEM images of (a) CBP:Eu, (b) CSPC:Eu, (c) NSP:Eu and (d) SAC:Eu (scale = 1 μm); the particle size distributions of (e) CBP:Eu, (f) CSPC:Eu and (g) NSP:Eu.

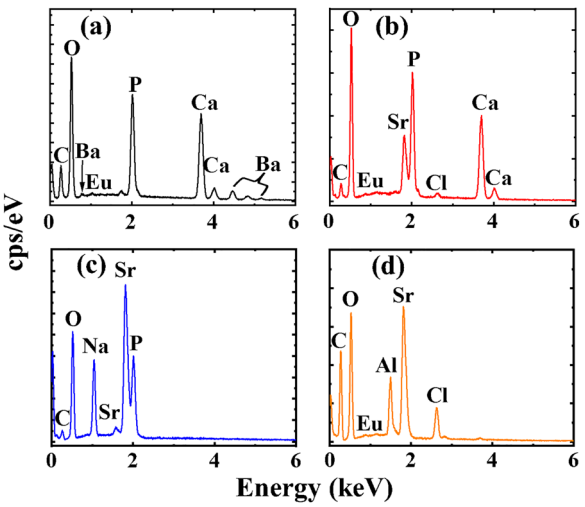

Fig. 4 EDS spectra of (a) CBP:Eu, (b) CSPC:Eu, (c) NSP:Eu and (d) SAC:Eu.

3.4. Temperature-dependent of luminescence

The temperature-dependent of the luminescence and lifetime of the phosphors were measured by exciting the phosphors using the third harmonic (355 nm, 10 ns, 10 Hz) of a Nd:YAG pulsed laser, Fig. 5. A 400 μm thick light sheet, with an energy density of 10 mJ cm^{-2}, was directed onto powder phosphor that was loaded into a copper block featuring a 2 mm wide hole. All measurements were performed in air in a dark room. The luminescence was recorded using a spectrometer, and the lifetime was recorded using a photodetector connected to an oscilloscope. The laser beam was converged onto the phosphor powder loaded on a copper block using cylindrical convex lenses (f = 50 mm). A temperature error of <2% was obtained for repeated (4×) lifetime measurements at 33.5 °C for all samples. Temperature errors can distort the calibration curve that links temperature to spectral output, such as intensity or lifetime. This can lead to poor accuracy and precision and may even cause the sensor to fail in high-temperature or reactive environments.

Table 2 Elemental compositions of the phosphors

	Elemental composition (wt%)			
Elements	CBP:Eu	CSPC:Eu	NSP:Eu	SAC:Eu
C	11.8	6.2	3.1	36.1
O	26.9	32.6	27.9	22.6
P	13.2	16.3	14.2	—
Ca	30.4	31.2	—	—
Ba	17.2	—	—	—
Cl	—	0.8	—	6.0
Sr	—	12.8	45.4	29.7
Na	—	—	9.1	—
Al	—	—	—	4.73
Eu	0.5	0.2	0.4	0.8

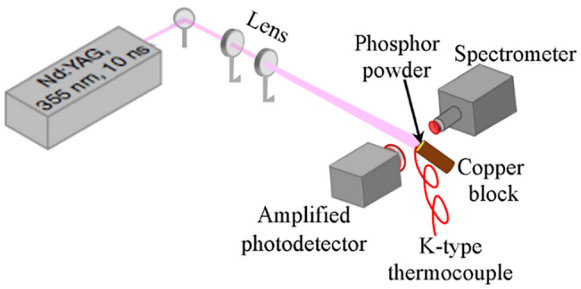

Fig. 5 Experimental setup for the temperature-dependent luminescent and lifetime measurements.

Eu^{2+} is one of the divalent rare earth ions that exhibit 5d–4f transitions (others include Sm^{2+} and Yb^{2+}, and trivalent ions such as Pr^{3+} and Ce^{3+}). These ions are fascinating because, depending on the activator ion environment in the host lattice, they can emit at different wavelength regions and form wide emission bands. The rationale behind the wide emission band is that the 5d–4f transitions are orbitally allowed according to the Laporte selection rule.[41] The tuning property of the emission wavelength of Eu^{2+} arises from the ability of energy separation between the 5d and 4f levels to change with variations in the crystal field strength of the host lattice.[42] Therefore, both excitation and emission bands shift to a longer wavelength with an increasing crystal field strength and *vice versa*.

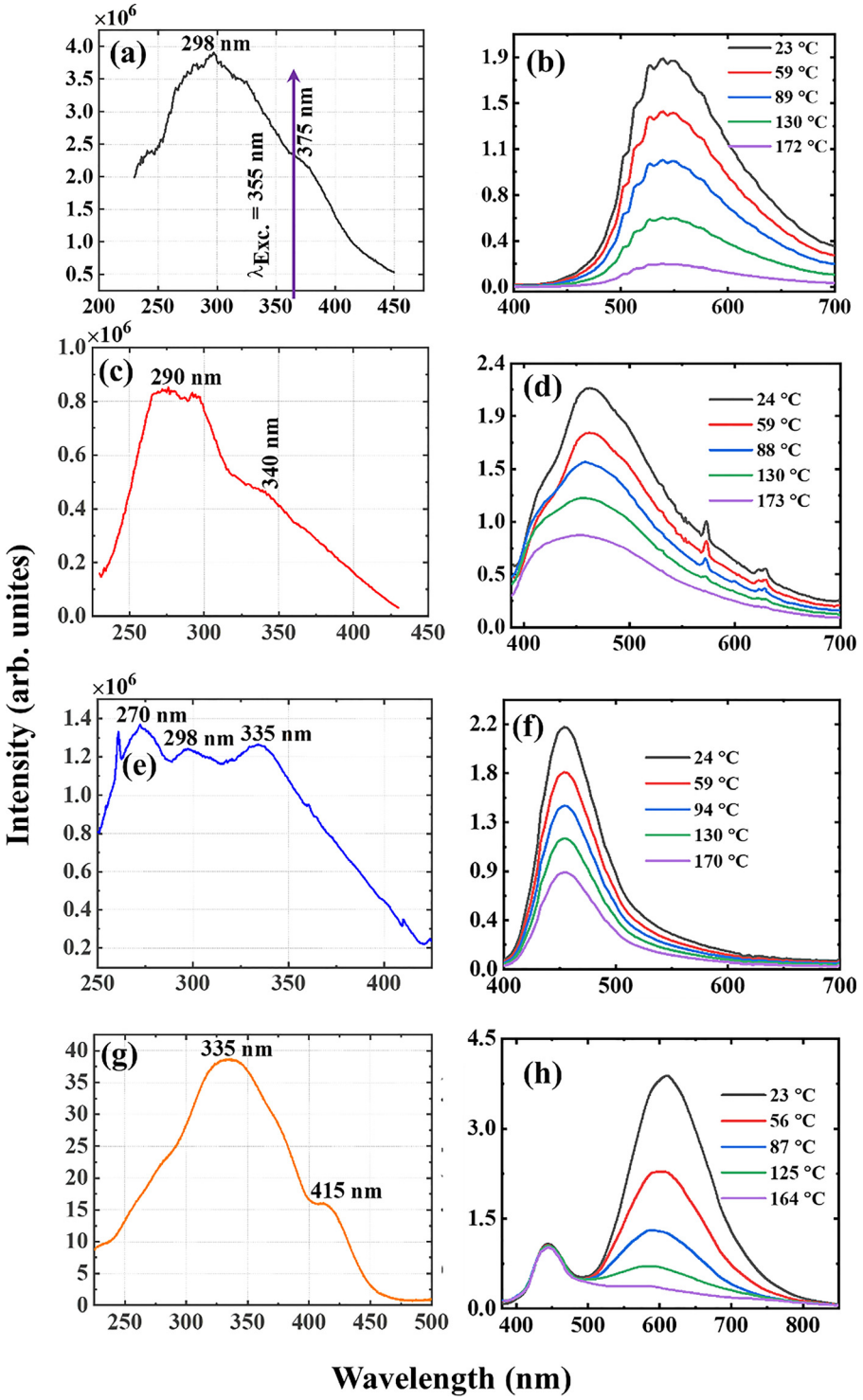

Fig. 6 The excitation spectra of (a) CBP:Eu, $\lambda_{Emi.}$ = 537 nm, (c) CSPC:Eu $\lambda_{Emi.}$ = 450 nm, (e) NSP:Eu, $\lambda_{Emi.}$ = 450 nm, (g) SAC:Eu, $\lambda_{Emi.}$ = 600 nm, and temperature-dependent emission spectra of (b) CBP:Eu (d) CSPC:Eu, (f) NSP:Eu, and (h) SAC:Eu, $\lambda_{Exi.}$ = 355 nm.

The excitation spectra of CBP:Eu, CSPC:Eu, NSP:Eu and SAC:Eu were measured using a fluorescence spectrometer under 537, 450, 450, and 600 nm emissions (Fig. 6(a, c, e and g), respectively). The excitation bands spread over the ultraviolet to the near-visible range of the electromagnetic spectrum, having maxima at 298, 290, 270, and 335 nm, respectively. CBP:Eu, CSPC:Eu, and SAC:Eu exhibited additional shoulders at 375, 340, and 415 nm, while NSP:Eu showed two additional peaks at 298 and 355 nm. These bands are assigned to the 4f–5d transitions of Eu^{2+}. It is evident from the excitation spectra that the phosphors can be excited effectively using 355 nm, which is convenient from a laser diagnostic perspective. The temperature

dependence of luminescence of CBP:Eu, CSPC:Eu, NSP:Eu and SAC:Eu was measured in the 23 to 173 °C temperature range, Fig. 6(b, d, f and h), respectively, using the third harmonic (355 nm) of a Nd:YAG laser.

The four samples exhibited emission maxima at 537, 450, 450, and 600 nm (with SAC:Eu possessing another band at 450 nm). These bands are assigned to the 5d–4f transitions of Eu^{2+}.[43,44] The peaks at 574 and 629 nm in Fig. 6(d) are assigned to the 4f–4f transitions of some unreduced Eu^{3+} in the matrix. From the normalized temperature-dependent emission spectra in Fig. S1(a–d), the emission bands broadened towards the blue with increasing temperature for all samples. The plots of the integrated emission intensities *versus* temperature are shown in Fig. S2(a–d).

The plots of the full-width-at-half-maxima (FWHM) of the phosphors, Fig. 7, increased with increasing temperature, except for CBP:Eu, which decreased up to 89 °C and then started to increase. The increase in the values of the FWHM can be attributed to increased lattice vibration of the materials with increasing temperature.[2] The behaviour observed at temperatures below 89 °C in CBP:Eu was reported in $SrMgAl_{10}O_{17}$:Eu and $CaSrSiO_4$:Eu,[45,46] and was attributed to two mechanisms:[46] (i) excited Eu^{2+} ions occupying the lower energy site tunnel to the higher energy site through a thermal phonons-activated assistant; (ii) emission from Eu^{2+} ions occupying the lower energy site quenches faster than the higher energy site due to thermally assisted energy back transfer from Eu^{2+} to the host.

The broad nature of these emission spectra suggests that they comprise multiple bands from Eu^{2+} ions occupying different sites in the hosts, as per the crystal structures in Fig. 2. CBP and CSPC have two sites, while SAC have three sites where Eu^{2+} can occupy. Emission from the Eu^{2+} occupying the Ba site in CBP can only be observed under a lower wavelength (300 nm) excitation.[8] The orthorhombic phase of NSP possesses three sites,[37] but the number of sites in the monoclinic phase is not known. However, it can be argued that both phases have a similar number of sites, since the PL emission spectra are similar. Eu^{2+} ions in the various sites emit distinct wavelengths due to the dependence of the 5d–4f transition on their environment, resulting in a combined broad emission band.

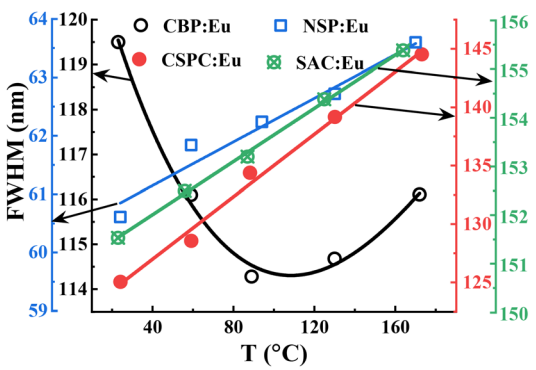

Fig. 7 FWHM of CBP:Eu, CSPC:Eu, NSP:Eu and SAC:Eu.

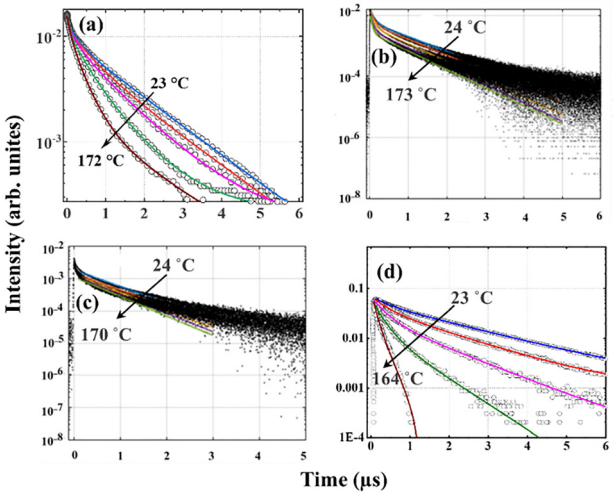

Fig. 8 Temperature-dependent of lifetimes of (a) CBP:Eu, (b) CSPC:Eu, (c) NSP:Eu and (d) SAC:Eu.

3.5. Temperature-dependent of lifetime

The temperature-dependent of lifetimes of CBP:Eu, CSPC:Eu, NSP:Eu and SAC:Eu measured within the temperature range of 23–173 °C using the 355 nm Nd:YAG laser as an excitation source, are shown in Fig. 8(a–d), respectively. The lifetime of the phosphors showed significant temperature-dependence, decreasing with increasing temperature. The decay curve of a material with luminescence intensity $I(t)$ at time t with an Nth order exponential decay is given by eqn (1)

$$I(t) = \sum_{i=1}^{N} A_i \exp\left(-\frac{t}{\tau_i}\right) \quad (1)$$

where τ_i and A_i are the decay times and amplitudes of the Nth exponential components of the luminescence decay, respectively.[47] The lifetimes of the samples were fitted using a double exponential equation, and the average lifetime, τ_{ave}, was determined using eqn (2)

$$\tau_{ave} = \frac{A_1\tau_1^2 + A_2\tau_2^2}{A_1\tau_1 + A_2\tau_2} \quad (2)$$

Similar to the temperature-dependent luminescence emission spectra. It is evident from Fig. 6 that the emission intensities of the four materials exhibit strong thermal quenching with temperature, but the lifetimes of CSPC:Eu and NSP:Eu (Fig. 8(b and c) showed weak temperature quenching. Similar results have been reported in different materials. In some cases, the luminescence intensity changes while the lifetime remains constant within the same temperature range;[48] in other cases, both parameters are quenched but at different rates,[49] while in other cases, they are quenched in different temperature ranges.[50] There are instances where the temperature-dependent of lifetime can provide information not available from luminescence data. Lifetime measurements can help distinguish between static and dynamic quenching.[51] In dynamic quenching, the quencher interacts with the excited state, influencing the

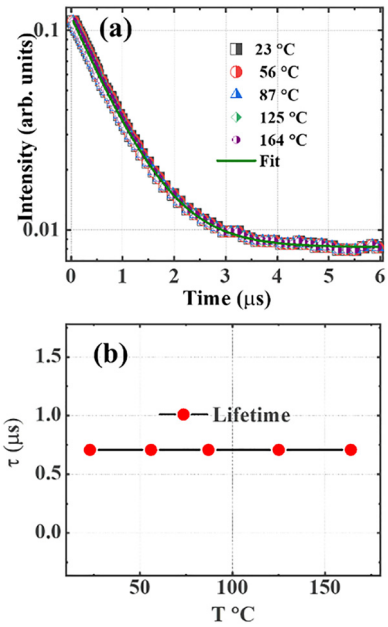

Fig. 9 (a) Temperature-dependent of lifetime of SAC:Eu when monitoring the 450 nm band using 355 nm excitation, and (b) the lifetime *versus* temperature.

entire population of excited electrons, which results in a decrease in luminescence intensity and average lifetime by reducing the probability of photon emission. On the other hand, in static quenching, the quencher forms a non-luminescent complex within the phosphors, thus reducing the number of active luminescent sites. Since the complex does not emit light, the lifetime of the uncomplexed phosphor remains the same, but the overall luminescence intensity drops due to fewer luminescent centres. The extent of static quenching depends on the amount of non-luminescent complex produced by the quencher.

The decay curves of the SAC:Eu measured by exciting the 450 nm band using the 355 nm Nd:YAG laser are markedly temperature independent in the measurement range of 23–164 °C, as shown in Fig. 9(a), which indicates that the radiative decay process dominates the transition. In this case, the lifetime parameter was extracted by fitting the luminescence decay curve using a single exponential function, which implies the presence of only one luminescent center. The luminescence lifetime was determined to be about 0.71 μs, and the plot of lifetime *versus* temperature, Fig. 9(b), showed an invariant lifetime behaviour with temperature change. Note that both the luminescence and lifetime of the 450 nm band can decrease at higher temperatures when thermal energy equals the activation energy of the band.

The cooling and heating cycles of the phosphors, shown in Fig. S3, demonstrated strong thermal stability and signal reproducibility within the measured temperature range.

3.6. Thermal quenching mechanism

On a mechanistic level, the general concept of thermal quenching of Eu^{2+}-doped phosphors exhibiting 4f–5d transitions is predominantly explained using one of the two following processes or a combination thereof: (1) non-radiative 5d–4f crossover relaxation through electron–phonon interaction, and (2) thermal ionization of the 5d electron of Eu^{2+} into the conduction band (CB) of the host.[52] These are described in detail below:

3.6.1. Non-radiative 5d–4f crossover relaxation. In this process, an excited electron of Eu^{2+} returns to the 4f ground state by means of vibrational relaxation. This is generally due to increased electron–phonon interaction when the temperature of a system is increased. When sufficient thermal energy, related to vibrational excitation near the Eu^{2+} ion within its excited state landscape, is provided, the 5d electron is elevated to the point where the 5d and 4f potential energy curves intersect in the configurational coordinate diagram (the red dots in Fig. 10(a) and (b)). Non-radiative relaxation takes place at the crossover point, and the energy required for this process is called the activation energy, ΔE. In CBP:Eu and CSPC:Eu, the excited energy levels (5d levels) of Eu^{2+} ions occupying the two Ca sites (Ca1 and Ca2) (representing the Sr site in CSPC:Eu with a Ca site for simplicity) are represented by the parabolas Ca1 and Ca2 in Fig. 10(a). The ΔE for Eu^{2+} ions occupying each Ca site is the energy difference between the bottom of the Ca parabola and its intersection with the 4f ground state parabola (indicated with red dots). For example, the ΔE_{Ca1} for Eu^{2+} ions occupying the Ca1 sites is indicated with the dotted blue lines in Fig. 10(a). In SAC:Eu, Eu^{2+} ions can occupy three different sites (Sr1, Sr2 and Sr3) and hence give rise to three excited energy levels represented by Sr1, Sr2 and Sr3 parabolas in Fig. 10(b). ΔE_{Sr1}, for example, is the activation energy of Eu^{2+} ions occupying the Sr1 site.

The total activation energy for thermal quenching in CBP:Eu and CSPC:Eu, ΔE_{Ca}, is given by eqn (3)

$$\Delta E_{Ca} = \Delta E_{Ca1} + \Delta E_{Ca2} \quad (3)$$

also, for NSP:Eu and SAC:Eu, the total activation energy is given by eqn (4)

$$\Delta E_{Sr} = \Delta E_{Sr1} + \Delta E_{Sr2} + \Delta E_{Sr3} \quad (4)$$

In SAC:Eu, ΔE_{Sr1} is considered constant because the luminescence intensity of Eu^{2+} in the Sr1 site did not show thermal

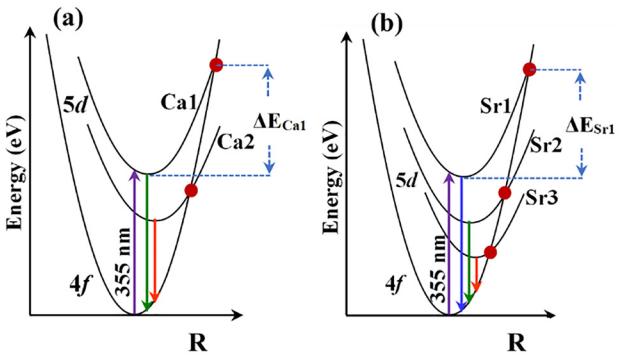

Fig. 10 Energy configuration diagrams of (a) CBP:Eu and CSPC:Eu, and (b) NSP:Eu and SAC:Eu illustrating the thermal quenching by considering the activation energy of Eu^{2+} energy levels.

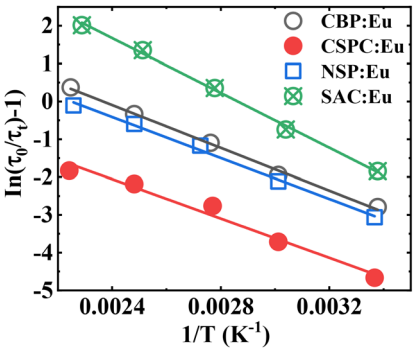

Fig. 11 The plot of the $\ln(\tau_0/\tau_T - 1)$ *versus* the inverse of temperature.

Table 3 The E_g, ΔE, ΔE_i and E_{5d} (Eu^{2+}, host) of the phosphors

Phosphors	ΔE (eV)	E_g (eV)	E_{5d} (Eu^{2+}, host)	ΔE_i (eV)
CBP:Eu	0.24	6.63[58]	6.39	0.24
CSPC:Eu	0.22	8.23[43]	8.10	0.13
NSP:Eu	0.23	6.80[60]	6.80	0.00
SAC:Eu	0.31	7.20[39]	7.09	0.11

quenching. The ΔE can be calculated from the temperature-dependent of lifetime data, Fig. 8, using a plot of the logarithm of $(\tau_0/\tau_T - 1)$ *versus* the inverse of the temperature in degrees Kelvin. In Fig. 11, the plot of $(\tau_0/\tau_T - 1)$ *versus* $1/T$ for the samples showed a linear regression. The activation energy can be calculated using the Arrhenius equation,[50,53] eqn (5)

$$\frac{-\Delta E}{k_B} \times \frac{1}{T} = \ln\left(\frac{\tau_0}{\tau_T} - 1\right) \quad (5)$$

where τ_0 is the initial lifetime (*e.g.*, 23 °C for SAC:Eu) and τ_T are the lifetimes at higher temperatures, k_B is the Boltzmann constant (8.629×10^{-5} eV K^{-1}). The value of ΔE can be calculated by equating the slope of the graph to $\Delta E/k_B$. The values of the activation energy for CBP:Eu, CSPC:Eu, NSP:Eu and SAC:Eu are listed in Table 3, with SAC:Eu having the largest ΔE value, while CSPC:Eu has the smallest values (see Fig. 13).

3.6.2. Thermal ionization. This mechanism describes the process where the 5d electron of the Eu^{2+} ion is thermally promoted to the CB of the host lattice, leading to the recombination of electron–hole pairs between the CB and the VB.[54] This delocalization of the electron results in a drop in the radiative recombination rate. Ionization energy (ΔE_i) is the energy required to promote a $5d_1$ electron to the conduction band minimum (CBM). ΔE_i can be determined from temperature-dependent photoconductivity measurement,[55] thermoluminescence,[56] or the Dorenbos semiempirical model.[57]

The Dorenbos semiempirical model uses the combination of spectroscopic data and an empirical model to determine a scheme containing all the divalent and trivalent lanthanide energy levels.[57] Fig. 12(a–d) shows the plot of the location of the energy levels of divalent and trivalent lanthanide ions in CBP, CSPC, NSP, and SAC host lattices, respectively. A piece of detailed information on how these energy levels were calculated

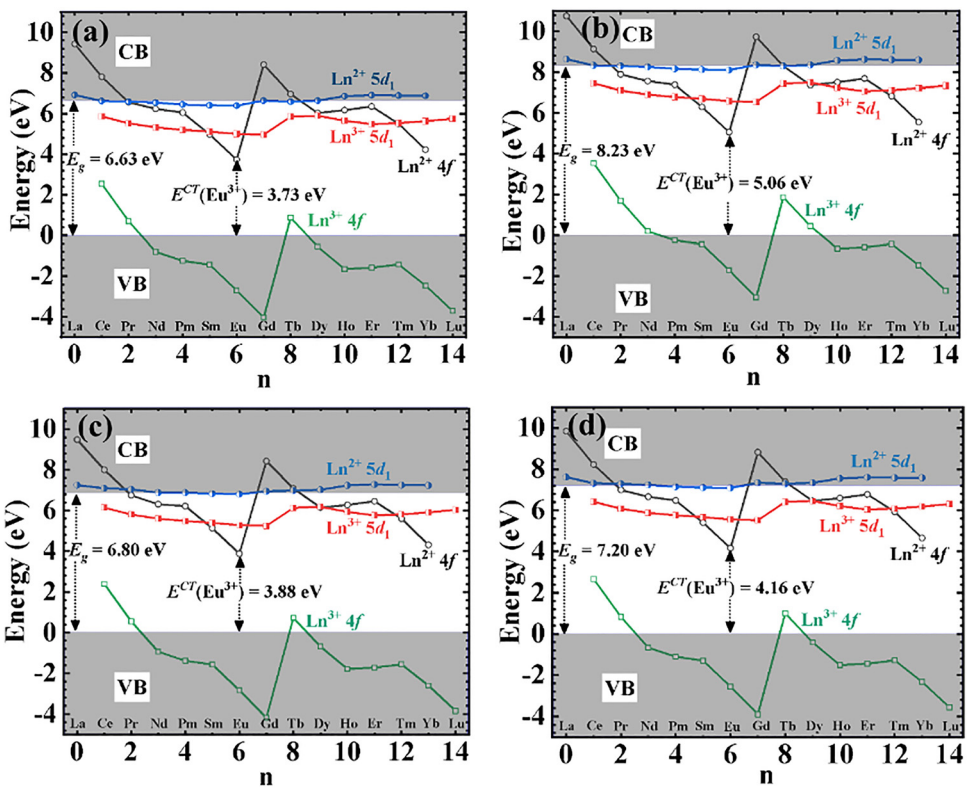

Fig. 12 Location of the energy levels of divalent and trivalent lanthanide ions in (a) CBP:Eu, (b) CSPC:Eu, (c) NSP:Eu, and (d) SAC:Eu.

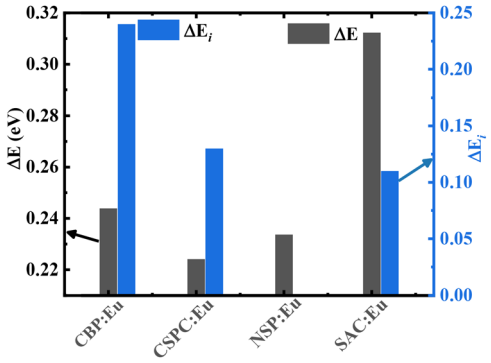

Fig. 13 The activation and ionization energy for CBP:Eu, CSPC:Eu, NSP:Eu and SAC:Eu.

is given in the supplementary information. The charge transfer band from O^{2-}–Eu^{3+}, E^{CT}, which is equivalent to the ground state of the Eu^{2+}, $E_{vf}(Eu^{2+}$, host), are 3.73,[58] 5.06, 3.88[59] and 4.16 eV, for CBP, CSPC, NSP, and SAC, respectively. The E^{CT} for CSPC and SAC were obtained from the PL excitation spectrum in Fig. S4(a) and (b), respectively. The values of the E_g, ΔE and ΔE_i are listed in Table 3. Fig. 13 shows the plot of ΔE and ΔE_i for the phosphors.

The values of ΔE and ΔE_i exhibited an irregular trend with one another. Among the materials, SAC:Eu exhibited the highest ΔE, while CBP:Eu demonstrated the highest ΔE_i. In contrast, CSPC:Eu and NSP:Eu had the lowest values for ΔE and ΔE_i, respectively. The irregularity in the variation of ΔE and ΔE_i could stem from the temperature at which each parameter was measured. ΔE is derived from luminescence thermal quenching at high temperatures, while ΔE_i is obtained from low temperatures. The temperature of the phosphor sample significantly influences the $5d_1$–CBM energy gap, since lattice thermal expansion leads to an increase in the $5d_1$ level while causing a decrease in the CBM.[61] Comparing the values of the ΔE and ΔE_i, it could be concluded that thermal ionization energy is the dominant mechanism for thermal quenching in CSPC:Eu, NSP:Eu, and SAC:Eu, due to the smaller values, while the rate of thermal ionization and non-radiative crossover relaxation are similar in CBP:Eu.

The energy level diagram of SAC:Eu was used as an example to illustrate the thermal ionization mechanism and the positions of Eu^{2+} energy levels relative to the host's, as shown in Fig. 14. In Fig. 14(a), the E_g of SAC is 7.20 eV[39] and the E^{CT}, which is equivalent to the 4f ground state energy level of Eu^{2+}, $E_{vf}(Eu^{2+}$, SAC), was determined to be 4.16 eV from the PL excitation spectrum of SAC:Eu^{3+} in Fig. S4(b). The excitation energy, 2.93 eV, is equivalent to the energy difference between the $E_{vf}(Eu^{2+}$, SAC) and the $5d_1$ states, $E_{5d}(Eu^{2+}$, SAC), of Eu^{2+} (the value of $5d_1$ is 7.09 eV, taken from row 6, column 8 of Table S8) as shown in the coordinate diagram in Fig. 14(b). These lead to the thermal ionization energy of 0.11 eV, which is the energy gap between the $5d_1$ excited state and the CBM, as shown in Fig. 14(a). The emission energy, 2.07 eV, was taken from the PL emission spectrum in Fig. 6(h).

3.7. Thermometric parameters and quantum yield

Temperature sensitivity is a crucial merit indicator in the area of application of an optical thermometer. For example,

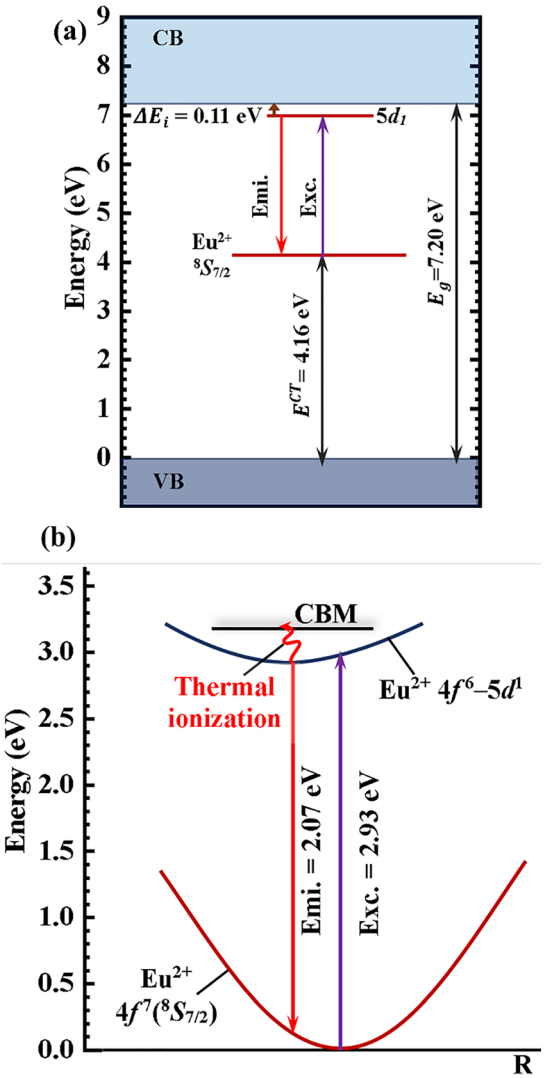

Fig. 14 (a) Constructed energy level diagram for Eu^{2+} ions relative to the VB and CB of the SAC host. (b) The configurational coordinate diagram showing the energy levels of Eu^{2+} relative to the conduction band minimum in SAC:Eu^{2+}.

materials used in high-temperature applications, such as in combustion engines, should be temperature-sensitive at ~1000 K (727 °C),[62] while materials used in low-temperature applications, such as in live cell imaging,[2] should be temperature-sensitive in the ambient range.

The relative temperature sensitivity, S_r, is defined by[53]

$$S_r = \left|\frac{1}{\tau(T)}\frac{d\tau(T)}{d(T)}\right| \times 100\% = \frac{A\exp\left(\frac{\Delta E}{k_B T}\right)}{1 + A\exp\left(\frac{\Delta E}{k_B T}\right)}\frac{\Delta E}{k_B T^2} \times 100\% \quad (6)$$

where $\tau(T)$ is the luminescence lifetime at a given temperature, $d\tau(T)/d(T)$ is the temperature derivative of $\tau(T)$, A is the rate constant, and k_B is the Boltzmann constant. From eqn (6), S_r is proportional to the ΔE and inversely related to the square of

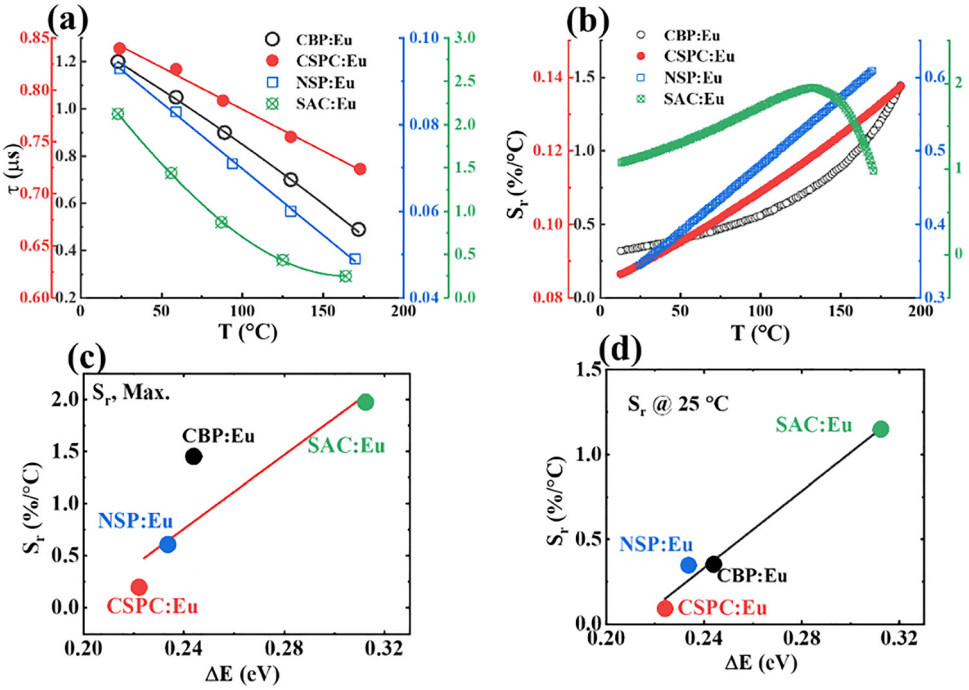

Fig. 15 Plot of (a) lifetime *versus* temperature, (b) relative sensitivity *versus* temperature, (c) maximum relative sensitivity *versus* activation energy, and (d) relative sensitivity at 25 °C *versus* activation energy.

temperature. Hence, materials with smaller ΔE tend to be thermally sensitive at low temperatures and *vice versa*. Therefore, the value of ΔE of a material also plays a crucial role in its thermometric application.

Fig. 15(a) shows the graph of the lifetimes of the phosphors *versus* temperature. It is evident that the lifetime quenches strongly within the temperature range of 23–173 °C. The S_r values calculated from the fitted data of Fig. 15(a) using eqn (6) are plotted *versus* temperature in Fig. 15(b). From Fig. 15(b), SAC:Eu has the highest maximum S_r value, (S_r,Max.), 1.97% °C^{-1} at 133 °C, followed by CBP:Eu, 1.45% °C^{-1}, at 172 °C, while NSP:Eu and CSPC:Eu have values of 0.61% °C^{-1} at 170 °C and 0.14% °C^{-1} at 173 °C, respectively (see Table 4).

To compare the temperature readout performance of the phosphors around ambient temperatures, values of S_r at 25 °C (S_r@25 °C) for all the samples are compared in Table 4. From the plot of S_r,Max. and S_r@25 °C *versus* ΔE in Fig. 15(c and d), respectively, the value of S_r increased with the ΔE, depicting their dependency. The values of the ionization energy, on the other hand, did not show regular correlation with the relative sensitivities, which is reasonable considering that ΔE and ΔE_i showed an irregular relationship in Fig. 13. SAC:Eu generally has the best temperature sensitivity, while CSPC:Eu has the poorest. Although CBP:Eu has a better sensitivity than NSP:Eu at higher temperatures, they have similar sensitivities around ambient temperatures.

Table 5 compares the maximum value of the lifetime-based S_r (S_r, max), the S_r value at 25 °C, and the lifetime at 25 °C of these phosphors to other phosphors in the literature. The S_r max of SAC:Eu compared very well to the best-reported values, except for $La_2MgGeO_6:Bi^{3+}$, Eu^{3+}. Also, around ~25 °C, SAC:Eu has a decent S_r value compared to $La_2MgGeO_6:Bi^{3+}$, Eu^{3+}. Materials with a very long decay time, >100 μs, or a very short decay time, <10 ns, are either very slow or very fast for imaging applications. The decay time of the reported phosphors is in the microsecond range, which can be detected using cameras with short interframe time, making it suitable for rapid imaging, such as in liquid and gas flows, where phosphors can be used as tracer particles.[40]

The temperature resolution, δT, defined by eqn (7), is the minimum detectable change in temperature that can detect the slightest change in the measured parameter value.[63]

$$\delta T = \frac{1}{S_r}\frac{\delta\tau}{\tau} \quad (7)$$

Table 4 Thermometric properties and the quantum yield of the phosphors

Phosphors	S_r@25 °C (% °C^{-1})	S_r,Max. (% °C^{-1})	$T_{S_r,Max.}$ (°C)	δT@25 °C	δT_{best}	$T_{\delta T_{best}}$ (°C)	QY (%)
CBP:Eu	0.349	1.452	172	0.05	0.01	172	19
CSPC:Eu	0.089	0.137	173	0.24	0.15	173	10
NSP:Eu	0.346	0.610	170	0.05	0.03	170	23
SAC:Eu	1.148	1.973	133	0.02	0.01	133	35

Table 5 Lifetime-based relative sensitivities of different phosphors and their lifetime at 25 °C

Phosphor	S_r,max%/°C	T (S_r,max) °C	S_r@25 °C	Tau@25 °C	$\lambda_{Exc.}$ (nm)	$\lambda_{Emi.}$ (nm)	Ref.
$Cd_3Al_2Ge_3O_{12}:Cr^{3+}$	1.40	−73	—	—	436	714	65
$Li_4GaSbO_6:Mn^{4+}$	2.82	77	1.40	440.00 (μs)	350	674	66
$NaBaBi_2(PO_4)_3:Eu^{3+}$	0.12	210	0.067@30 °C	2.22 (ms)@30 °C	394	613	67
$Sr_4GaNbO_8:Mn^{4+}$	3.34	120	3.08@30 °C	135.60 (μs)@30 °C	350	716	68
$Na_3Sc_2(PO_4)_3:Yb^{3+}$	1.20	82	—	—	940	980	69
$KSrGdTeO_6:Mn^{4+}$	2.3233	175	0.25@50 °C	0.20 (ms) @50 °C	346	670	70
$Ba_3LuGa_2O_{7.5}:Bi^{3+}$	2.21	50	1.64	335.43 (ns)	351	500	71
$Ca_4(PO_4)_2O:Eu^{2+},Eu^{3+}$	2.07	20	2.00	0.80 (μs)	355	700	61
$InTaO_4:Cr^{3+}$	2.27	42	1.42	4.58 (μs)	500	880	72
$Sr_4Al_{14}O_{25}:Mn^{4+}$	1.50	147	0.21	1.55 (ms)	400	651	73
$Nd_{0.5}Y^{3+}{}_{0.4}Yb_{0.1}PO_4$	1.22	82	1.14	0.11 (ms)	808	980	74
$Nd_{0.5}Lu^{3+}{}_{0.4}Yb_{0.1}PO_4$	0.85	127	0.71	0.12 (ms)	808	980	74
$Nd_{0.5}La^{3+}{}_{0.4}Yb_{0.1}PO_4$	1.05	147	0.84	0.16 (ms)	808	980	74
$Nd_{0.5}Gd^{3+}{}_{0.4}Yb_{0.1}PO_4$	0.74	172	0.45	0.09 (ms)	808	980	74
$Zn_{0.9}Mn_{0.1}Al_2O_4:Cr^{3+}$	0.80	−13	0.78	0.04 (ms)	427	512	75
$ZnGa_2O_4:Cr^{3+}{}_{0.5\%},Bi^{3+}{}_{0.5\%}@SiO_2$	1.93	200	0.41	2.00 (ms)	430	692	76
$SrZrO_3:Eu^{3+}$	0.30	187	0.01	0.45 (ms)	237	616	77
$ZnGa_2O_4:Cr^{3+}$	0.58	147	0.20	4.17 (ms)	406	684	78
$LiGa_5O_8:Cr^{3+}$	0.76	22	0.74	2.50 (ms)	406	684	78
$Ga_2O_3:Cr^{3+}$	0.46	97	0.35	1.11 (ms)	406	684	78
$La_2MgGeO_6:Bi^{3+},Eu^{3+}$	4.09	110	1.12	0.33 (μs)	333	402	79
$Ba_2LaNbO_6:Mn^{4+}$	2.77	134	0.25@27 °C	0.22 (ms)	332	681	80
$Ca_2SiO_4:Mn^{2+}$	4.25	102	1.55	16.00 (ms)	365	550	81
$Mg_2TiO_4:Cr^{3+}$	0.75	157	0.41	1.38 (ms)	473	712	82
$Bi_2Ga_4O_9:Cr^{3+}$	1.60	450	0.42	20 (μs)	355	775	83
$ScVO_4$:1%Bi^{3+}	2.83	49	2.52	2.12 (μs)	355	600	84
YVO_4:1%Bi^{3+}	2.34	191	0.00	3.92 (μs)	355	545	84
$Sr_2V_2O_7$:0.001Bi^{3+}	2.56	20	2.13	3.85 (μs)	355	540	85
$Li_4SrCa(SiO_4)_2:Eu^{2+}$	15.00	300	1.00@30 °C	200.00 (ns)	363	433	86
$LaSc_3(BO_3)_4:Eu^{2+}/Eu^{3+}$	7.68	−23	3.50	∼5.00 (ns)	345	455	87
$SrB_4O_7:Eu^{2+}$	10.50	−252	0.02	10.00 (μs)	300	362.4	88
CBP:Eu	1.45	172	0.349	1.19 (μs)	355	537	TW
CSPC:Eu	0.14	173	0.089	0.82 (μs)	355	450	TW
NSP:Eu	0.61	170	0.346	0.09 (μs)	355	450	TW
SAC:Eu	1.97	133	1.148	1.81 (μs)	355	600	TW

N/B: TW = this work.

where $\delta\tau/\tau$ is the relative standard error in determining the lifetime, and was determined by calculating the standard deviation from 10 measurements of each phosphor's decay time at a fixed temperature.[64]

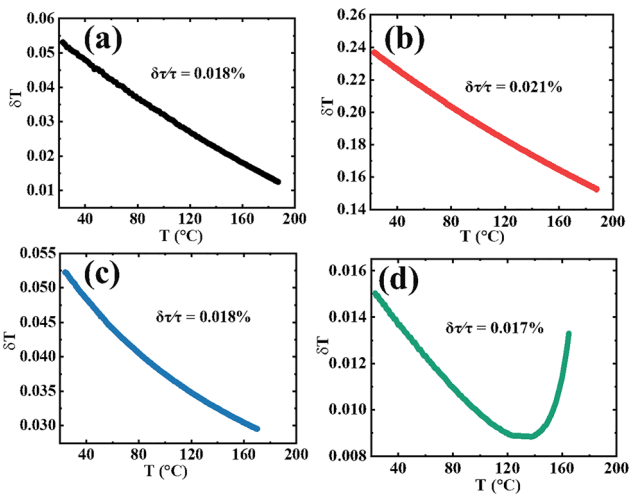

Fig. 16 Temperature resolutions of (a) CBP:Eu, (b) CSPC:Eu, (c) NSP:Eu and (d) SAC:Eu.

Fig. 16(a–d) shows the plot of the temperature resolution of CBP:Eu, CSPC:Eu, NSP:Eu and SAC:Eu, respectively. The values of the best resolution (δT_{best}), the corresponding temperature ($T_{\delta T_{best}}$), and the resolution at 25 °C (δT@25 °C) for all samples are listed in Table 4. SAC:Eu has the overall best resolution, followed by CBP:Eu and NSP:Eu, while CSPC:Eu has the least resolution.

The quantum yields (QYs) of CBP:Eu, CSPC:Eu, NSP:Eu, and SAC:Eu were measured under 375, 295, 270, and 332 nm excitations, respectively, and are listed in Table 4. The QY values range from 10% to 35%, with SAC:Eu having the highest value, followed by CBP:Eu, and CSPC:Eu with the lowest. SAC:Eu exhibited the highest QY and room temperature relative sensitivity, which is over three times higher than that of the other phosphors, making it the overall best performer among them.

4. Conclusion

Four thermometric phosphors, CBP:Eu, CSPC:Eu, NSP:Eu, and SAC:Eu, were prepared, and their thermometric properties were compared. The activation energy (ΔE) values and the thermal ionization energy (ΔE_i) of the phosphors were determined.

The values of the ΔE increased in the order SAC:Eu > CBP:Eu > NSP:Eu > CSPC:Eu and exhibited an irregular relationship with the ΔE_i. Thermal ionization is the dominant mechanism for thermal quenching in CSPC:Eu, NSP:Eu and SAC:Eu, whereas the rates of thermal ionization and non-radiative crossover relaxation are identical in CBP:Eu. In addition, the maximum values of the relative temperature sensitivities (S_r,Max.) exhibited a linear relationship with the ΔE. This suggests that to obtain a high S_r, the value of ΔE should be maximized. Also, the quantum yield increased in the order SAC:Eu > NSP:Eu > CBP:Eu > CSPC:Eu. In general, SAC:Eu offered the best overall performance in terms of temperature sensitivity, resolution, and quantum yield, while CBP:Eu and NSP:Eu offered relatively similar values, and CSPC:Eu produced the poorest values. Nevertheless, all the phosphors exhibited temperature sensitivity at ambient temperatures, and their lifetimes are in the microsecond range, making them suitable for temperature imaging of fast-moving objects, *e.g.* fluid temperature imaging.

Author contributions

Hendrik C. Swart: funding acquisition, supervision, resources and writing – review & editing. Robin E. Kroon: supervision, resources and writing – review & editing. Simon N. Ogugua: writing – original draft, conceptualization, investigation, methodology and validation, visualization.

Conflicts of interest

There are no conflicts to declare.

Data availability

The data supporting the findings of this study are available in the supplementary information (SI) of this article. Supplementary information is available. See DOI: https://doi.org/10.1039/d5ma01397f.

Acknowledgements

South African Research Chairs Initiative of the Department of Science and Innovation and the National Research Foundation of South Africa (84415). National Research Foundation of South Africa (Grant Number 93214, R.E. Kroon) for photoluminescence measurements. The authors thank Lehrstuhl für Technische Thermodynamik, Otto-von-Guericke-Universität Magdeburg, 39106 Magdeburg, and the World Academy of Sciences/Deutsche Forschungsgemeinschaft (AB668/1-1).

References

1 Transparency Market Research Inc., 02/12/2024, https://www.powersystemsdesign.com/articles/temperature-sensor-market-set-to-surge-at-5-4-cagr-to-reach-usd-10-1-billion-by-2031/29/21224.
2 K. Okabe, N. Inada, C. Gota, Y. Harada, T. Funatsu and S. Uchiyama, *Nat. Commun.*, 2012, **3**, 705.
3 M. Monti, L. Brandt, J. Ikomi-Kumm and H. Olsson, *Scand. J. Haematol.*, 1986, **36**, 353–357.
4 B. del Rosal, D. Ruiz, I. Chaves-Coira, B. H. Juárez, L. Monge, G. Hong, N. Fernández and D. Jaque, *Adv. Funct. Mater.*, 2018, **28**, 1806088.
5 M. Mansoora, I. Haneef, S. Akhtar, A. De Lucac and F. Udrea, *Sens. Actuators, A*, 2015, **232**, 63–74.
6 P. R. N. Childs, J. R. Greenwood and C. A. Long, *Rev. Sci. Instrum.*, 2000, **71**, 2959–2978.
7 J. J. Carvajal and M. C. Pujol, Introduction to Luminescence Thermometry, ed. J. J. C. Martí and M. C. P. Baiges, in *Luminescent Thermometry: Applications and Uses*, Springer Nature, Cham, Switzerland, 2023, pp. 1–68.
8 R. Zhou, C. Liu, L. Lin, Y. Huang and H. Liang, *Chem. Eng. Sci.*, 2019, **369**, 376–385.
9 S. C. Lal, I. N. Jawahar and S. Ganesanpotti, *J. Sci. Adv. Mater Dev.*, 2023, **8**, 100544.
10 Y. Xue, Y. Chen, G. Li, W. Xia, Q. Mao, L. Pei, M. Liu, L. Chu and J. Zhong, *Chin. Chem. Lett.*, 2024, **35**, 108447.
11 Y. Chen, F. Zhao, K. Qiang, Q. Mao, H. Yang, Y. Zhu, M. Liu and J. Zhong, *Adv. Opt. Mater.*, 2024, **12**, 2401688.
12 L. Liang, H. Yang, Q. Mao, F. Zhao, Y. Ding, X. Li, M. Liu and J. Zhong, *Chem. Eng. J.*, 2025, **508**, 161129.
13 A. Bindhu, J. I. Naseemabeevi and S. Ganesanpotti, *Adv. Photonics Res.*, 2022, **3**, 2100159.
14 L. Marciniak, K. Kniec, K. Elżbieciak-Piecka, K. Trejgis, J. Stefanska and M. Dramićanin, *Coord. Chem. Rev.*, 2022, **469**, 214671.
15 C. D. S. Brites, R. Marin, M. Suta, A. N. C. Neto, E. Ximendes, D. Jaque and L. D. Carlos, Spotlight on Luminescence Thermometry: Basics, Challenges, and Cutting-Edge Applications, *Adv. Mater.*, 2023, **35**, 2302749.
16 G. Hong, S. Diao, J. Chang, A. L. Antaris, C. Chen, B. Zhang, S. Zhao, D. N. Atochin, P. L. Huang, K. I. Andreasson, C. J. Kuo and H. Dai, *Nat. Photonics*, 2014, **8**, 723–730.
17 G. Liebsch, I. Klimant, B. Frank, G. Holst and O. S. Wolfbeis, *Appl. Spectrosc.*, 2000, **54**, 548–559.
18 X. Wang, O. S. Wolfbeis and R. J. Meier, *Chem. Soc. Rev.*, 2013, **42**, 7834–7869.
19 L. Shang, F. Stockmar, N. Azadfar and G. U. Nienhaus, *Angew. Chem., Int. Ed.*, 2013, **52**, 11154–11157.
20 W. Becker, *J. Microsc.*, 2012, **247**, 119–136.
21 T. Kissel, E. Baum, A. Dreizler and J. Brübach, *Appl. Phys. B*, 2009, **96**, 731–734.
22 V. Bachmann, C. Ronda, O. Oeckler, W. Schnick and A. Meijerink, *Chem. Mater.*, 2009, **21**, 316–325.
23 M. A. Reshchikov, *Phys. Status Solidi A*, 2021, **218**, 2000101.
24 M. Müller, M.-F. Volhard and T. Jüstel, *RSC Adv.*, 2016, **6**, 8483–8488.
25 S. N. Ogugua, C. Abram, B. Fond, R. E. Kroon, F. Beyraud and H. C. Swart, *Dalton Trans.*, 2024, **53**, 4551–4563.
26 R. Shafei, D. Maganas, P. J. Strobel, P. J. Schmidt, W. Schnick and F. Neese, *J. Am. Chem. Soc.*, 2022, **144**, 8038–8053.

27 S. N. Ogugua, H. C. Swart and O. M. Ntwaeaborwa, *Sens. Actuators, B*, 2017, **250**, 285–299.
28 T. Kang, S. Lee, T. Kim and J. Kim, *Sci. Rep.*, 2020, **10**, 1475.
29 Y. Jia, A. Miglio, M. Mikami and X. Gonze, *Phys. Rev. Mater.*, 2018, **2**, 125202.
30 J. Zheng, S. Wu, G. Chen, S. Dang, Y. Zhuang, Z. Guo, Y. Lu, Q. Cheng and C. Chen, *J. Alloys Compd.*, 2016, **663**, 332–339.
31 D. K. Yim, H. J. Song, I.-S. Cho, J. S. Kim and K. S. Hong, *Mater. Lett.*, 2011, **65**, 1666–1668.
32 S. N. Ogugua, S. K. K. Shaat, H. C. Swart, R. E. Kroon and O. M. Ntwaeaborwa, *J. Alloys Compd.*, 2019, **775**, 950–968.
33 N. Komuro, M. Mikami, Y. Shimomura, E. G. Bithell and A. K. Cheetham, *J. Mater. Chem. C*, 2014, **2**, 6084–6089.
34 R. D. Shannon, *Acta Cryst.*, 1979, **A32**, 751–767.
35 J. Wen, Y. Wang, G. Jiang, J. Zhong, J. Chu, Q. Xia, Q. Zhang, L. Ning, C.-K. Duan and M. Yin, *Inorg. Chem.*, 2020, **59**, 5170–5181.
36 G. Nénert, *Acta Cryst.*, 2021, **A77**, C636.
37 The Materials Project. Materials data on NaSrPO4 by Materials Project. United States: N.p., 2020, DOI: 10.17188/1736564.
38 A. Balakrishna and O. M. Ntwaeaborwa, *Sens. Actuators, B*, 2017, **242**, 305–317.
39 L. Ning, C. Zhou, W. Chen, Y. Huang, C. Duan, P. Dorenbos, Y. Tao and H. Liang, *J. Phys. Chem. C*, 2015, **119**, 6785–6792.
40 C. Abram, I. W. Panjikkaran, S. N. Ogugua and B. Fond, *Opt. Lett.*, 2020, **45**, 3893–3896.
41 M. Gaft, R. Reisfeld and G. Panczer, Theoretical Background, in *Modern luminescence spectroscopy of minerals and materials*, Springer International Publishing, Switzerland, 2nd edn, 2015, pp. 9–32.
42 T. Justel, W. Mayr and P. J. Schmidt, Tuning the 4f15d-4f2 UV emission of Pr3+, in Proc. 200th Meeting of the Electrochemical Society, San Francisco, CA, USA, September 2001.
43 L. Wang, K. Liu, J. Wang, L. Zhao, Y. Xu, R. Zhou, L. Chen and B. Qu, *Opt. Mater.*, 2020, **107**, 110014.
44 W. Zhou, J. Han, X. Zhang, Z. Qiu, Q. Xie, H. Liang, S. Lian and J. Wang, *Opt. Mater.*, 2015, **39**, 173–177.
45 H. Tanno, S. Zhang, T. Shinoda and H. Kajiyama, *J. Lumin.*, 2010, **130**, 82–86.
46 H.-J. Woo, M. Jayasimhadri and K. Jang, *J. Alloys Compd.*, 2017, **703**, 80–85.
47 J. Włodarczyk and B. Kierdaszuk, *Biophys. J.*, 2003, **85**, 589–598.
48 A. R. Beck, S. Das and J. Manam, *J. Mater. Sci.: Mater. Electron.*, 2017, **28**, 17168–17176.
49 L. Wang, Y. Zhang, D. Gao, X. Sha, X. Chen, Y. Zhang, J. Zhang, X. Zhang, Y. Cao, Y. Wang, X. Li, S. Xu, H. Yu and B. Chen, *Results Phys.*, 2024, **56**, 107238.
50 T. Senden, R. J. A. van Dijk-Moes and A. Meijerink, *Light: Sci. Appl.*, 2018, **7**, 8.
51 J. R. Lakowicz, Time-Domain Lifetime Measurement, *Principles of Fluorescence Spectroscopy*, Springer Science + Business Media, USA, 3rd edn, 2006, p. 97.
52 Y.-C. Lin, M. Bettinelli and M. Karlsson, *Chem. Mater.*, 2019, **31**, 3851–3862.
53 T. Lu, Z. Ma, C. Du, Y. Fang, H. Wu, Y. Jiang, L. Wang, L. Dai, H. Jia, W. Liu and H. Chen, *Sci. Rep.*, 2014, **4**, 6131.
54 S. Schmiechen, H. Schneider, P. Wagatha, C. Hecht, P. J. Schmidt and W. Schnick, *Chem. Mater.*, 2014, **26**, 2712–2719.
55 E. van der Kolk, S. A. Basun, G. F. Imbusch and W. M. Yen, *Appl. Phys. Lett.*, 2003, **83**, 1740–1742.
56 J. Ueda, P. Dorenbos, A. J. J. Bos, A. Meijerink and S. Tanabe, *J. Phys. Chem. C*, 2015, **119**, 25003–25008.
57 F. You, A. J. J. Bos, Q. Shi, S. Huang and P. Dorenbos, *Phys. Rev. B*, 2012, **85**, 115101.
58 L. Ning, X. Huang, J. Sun, S. Huang, M. Chen, Z. Xia and Y. Huang, *J. Phys. Chem. C*, 2016, **120**, 3999–4006.
59 D. G. Lee, S. K. Singh, C. H. Moon, S. S. Yi, K. Jang, D.-S. Shin, J. H. Jeong and J.-S. Bae, *J. Nanosci. Nanotechnol.*, 2013, **13**, 5552–5555.
60 L. Xiong, L.-M. Wu and L. Chen, *Angew. Chem. Int. Ed.*, 2021, **60**, 25063–25067.
61 S. Yan, *J. Rare Earths*, 2020, **38**, 113–123.
62 J. W. Kenney and J. J. Lee, *Chemosens*, 2021, **9**, 109.
63 M. D. Dramićanin, *Rev. Methods. Appl. Fluoresc.*, 2016, **4**, 42001.
64 S. N. Ogugua, L. J. B. Erasmus and H. C. Swart, *Mater. Res. Bull.*, 2023, **164**, 112256.
65 Z. Yang, W. Zhang, Z. Wang, Y. Zheng, Y. Su, H. Xu, Z. Guo, R. Wang and S. Yang, *J. Alloys Compd.*, 2025, **1022**, 179931.
66 K. Li, Z. Huang and D. Zhu, *Ceram. Int.*, 2025, **51**, 17433–17444.
67 K. J. Albert and S. M. M. Kennedy, *J. Lumin.*, 2025, **280**, 121122.
68 Z. Huang, K. Li, Z. Zhang, J. Liu and D. Zhu, *J. Mater. Chem. C*, 2025, **13**, 4564.
69 A. Javaid, M. Szymczak, M. Kubicka, J. Zeler, V. Kinzhbalo, M. Drozb, D. Szymanski and L. Marciniak, *J. Mater. Chem. C*, 2025, **13**, 9174–9184.
70 M.-H. Yu, D. Zhao, R.-J. Zhang, Q.-X. Yao, L. Jia and Q. Zong, *Ceram. Int.*, 2024, **50**, 11766–11775.
71 R. Liu, H. Wu, S. Wang, W. Yuan, S. Zhang, R. Pang, L. Jiang, D. Li, C. Li and H. Zhang, *J. Mater. Chem. C*, 2023, **11**, 2653–2663.
72 L. Qiu, P. Wang, J. Mao, Z. Liao, F. Chi, Y. Chen, X. Wei and M. Yin, *Inorg. Chem. Front.*, 2022, **9**, 3187–3199.
73 M. Pieprz, W. Piotrowski, P. Wózny, M. Runowski and L. Marciniak, *Adv. Opt. Mater.*, 2024, **12**, 2301316.
74 K. Maciejewska, A. Bednarkiewicz and L. Marciniak, *Nanoscale Adv.*, 2021, **3**, 4918–4925.
75 S. Ren, Y. Wu, Q. Wang, B. Yang, Q. Shi, S. Li and D. Zhang, *J. Lumin.*, 2022, **251**, 119264.
76 E. Glais, M. Pellerin, V. Castaing, D. Alloyeau, N. Touati, B. Viana and C. Chanéac, *RSC Adv.*, 2018, **8**, 41767–41774.
77 S. Das, S. Som, C.-Y. Yang, S. Chavhan and C.-H. Lu, *Sci. Rep.*, 2016, **6**, 25787.
78 D. Chen, Z. Wan, Y. Zhou and Z. Ji, *J. Eur. Ceram. Soc.*, 2015, **35**, 4211–4216.
79 Y. Chen, Y. Shen, L. Zhou, J. Lin, J. Fu, Q. Fang, R. Ye, Y. Shen, S. Xu, L. Lei and D. Deng, *J. Lumin.*, 2022, **249**, 118995.
80 W. Wang, Q. Li, L. Chen, Y. Wang, R. Zhong, H. Dong, Y. Qiu, Y. Hu and X. Zhang, *J. Lumin.*, 2023, **257**, 119683.
81 X. Fan, W. Zhang, F. Lü, Y. Sui, J. Wang and Z. Xu, *Sensors*, 2021, **12**, 2788.

82 Z. Ristić, V. Đorđević, M. Medić, S. Kuzman, M. G. Brik, Ž. Antić and M. D. Dramićanin, *Opt. Mater.*, 2021, **120**, 111468.
83 M. Back, J. Ueda, M. G. Brik, T. Lesniewski, M. Grinberg and S. Tanabe, *ACS Appl. Mater. Interfaces*, 2018, **10**, 41512–41524.
84 S. Hirsch, M. Elashry, N. Fdida, C. Irimiea, S. Petit, G. Pilla, U. Betke, A. Rashed, C. Abram and B. Fond, *Adv. Opt. Mater.*, 2025, e01978.
85 S. N. Ogugua, L. J. B. Erasmus, R. E. Kroon and H. C. Swart, *J. Mater. Chem. C*, 2024, **12**, 18481–18492.
86 M. Wu, D. Deng, F. Ruan, B. Chen and S. Xu, *Chem. Eng. J.*, 2020, **396**, 125178.
87 N. Yang, Z. Li, T. Zhou, Z. Zhang, W. Shi, Y. Tong and J. Shi, *J. Adv. Ceram.*, 2024, **13**, 821–833.
88 M. Sójka, M. Runowski, T. Zheng, A. Shyichuk, D. Kulesza, E. Zych and S. Lis, *J. Mater. Chem. C*, 2022, **10**, 220–1227.